Nano Research Energy

ISSN 2791-0091 (print); 2790-8119 (online)
https://doi.org/10.26599/NRE.2025.9120215

Research Article

Interfacial electronic modulation by single-atom metals in nitrogen-doped carbon on Co_3O_4 for acidic oxygen evolution

Zhiyi Sun[1], Chen Li[2], Zhiwei Zhao[1], Kun Zheng[2] (✉), and Zhuo Chen[1] (✉)

[1] *Energy & Catalysis Center, School of Materials Science and Engineering, Beijing Institute of Technology, Beijing 100081, China*
[2] *Beijing Key Laboratory of Microstructure and Property of Solids, Faculty of Materials and Manufacturing, Beijing University of Technology, Beijing 100124, China*

Received: 26 October 2025 / **Revised:** 9 December 2025 / **Accepted:** 13 December 2025 / **Published date:** 19 January 2026

ABSTRACT

Non-precious metal-based catalysts for the acidic oxygen evolution reaction (OER) offer great potential due to their continuously improving performance, earth abundance and low cost. However, their catalytic activity and stability remain inadequate for practical applications. Here we implement an interfacial modulation strategy by coating cobalt oxide (e.g., Co_3O_4) nanocrystals with a single-metal-atom–modified, nitrogen-doped carbon (MNC) layer, and further optimize the interface between Co_3O_4 and MCN through single atom metal regulation. Across the series, Co_3O_4/MnNC exhibits a trend-like optimum, delivering overpotentials of 296 and 401 mV at 10 and 100 mA·cm^{-2}, respectively, and showing excellent durability with only a 36 mV increase after 240 h at 10 mA·cm^{-2}. Combining X-ray absorption fine structure (XAFS) characterization and density functional theory (DFT) calculations, the Co–N–Mn structure is identified as the active site, while the coating layer suppresses surface structural relaxation of Co_3O_4, thereby improving the structural stability. Moreover, *in situ* XAFS investigations confirm the formation of a stable Co–N–Mn interfacial structure under operational conditions. These results offer interfacial modulation as an effective route for high-performance, earth-abundant OER catalysts in acidic media.

KEYWORDS

acidic oxygen evolution reaction, Co_3O_4, N-doped carbon, single metal atom catalyst, interfacial modulation

1 Introduction

The acidic oxygen evolution reaction (OER) is a vital process in proton exchange membrane water electrolysis (PEMWE), providing a promising and environmentally sustainable approach to modern energy conversion and storage [1–4]. However, the acidic OER is a multi-step process involving the transfer of four electrons and protons, which inherently exhibits sluggish kinetics that result in high overpotentials [5–7]. While noble metal-based materials such as Ir and Ru have demonstrated exceptional performance in acidic OER, their high cost and limited availability significantly impede large-scale commercial adoption [8, 9]. In recent years, substantial efforts have focused on developing non-noble-metal-based catalysts for acidic OER, aiming to achieve low overpotentials for multi-electron coupling while maintaining high stability [10–14]. Cobalt oxides (e.g., Co_3O_4) are promising alternatives to noble metals for OER applications due to their elemental abundance and high catalytic activity [15–17]. However, the performance of cobalt oxide, in terms of both overpotential and durability, still requires further improvement to meet the demands of practical applications.

Various strategies have been reported to enhance the overall performance of cobalt oxide catalysts for efficient and stable operation in acidic OER [18–22]. These approaches primarily include: (1) tuning the electronic band structure, charge transfer pathways, and coordination environment of active sites in Co_3O_4 by introducing metal elements (such as transition metals and rare earth metals) or non-metal elements (such as halogens and light elements) [23–28]. thereby synergistically enhancing intrinsic catalytic activity and electrochemical stability; (2) modulating the local electronic state density on the catalyst surface by creating oxygen vacancies, anchoring metal vacancies, or inducing lattice strain to optimize the adsorption–desorption kinetics of key intermediates (e.g., *OOH) [29, 30]; and (3) fabricating heterostructures or composite materials to design specific reaction interfaces that enhance charge transfer efficiency through synergistic effects [31]. Despite these advances, overall catalytic performance remains suboptimal due to frequent valence state changes and surface reconstruction during operation [32–34]. Moreover, under practical conditions, the evolution of interfacial structures and valence states at reaction sites remains inadequately understood, impeding deeper insights into the reaction mechanism.

Address correspondence to Kun Zheng, kunzheng@bjut.edu.cn; Zhuo Chen, zchen@bit.edu.cn

Single-atom catalysts provide atomically dispersed, well-defined sites, enabling precise links between the local microenvironment and catalytic performance [35–37]. This work develops an interfacial engineering strategy that enables the synergistic modulation of Co_3O_4 nanocatalyst, significantly reducing its overpotential while substantially enhancing catalytic stability. The strategy involves: (1) constructing a metal single-atom nitrogen-doped carbon coating layer on the surface of Co_3O_4; (2) tuning interface (Co–N–M) at Co surface sites by regulating the single-atom metal, thereby improving performance; and (3) mitigating surface structural relaxation through the coating layer to improve structural stability and identifying Co–N–Mn as the active site. The effect of coating coverage on catalytic performance was systematically investigated and further elucidated through X-ray absorption fine structure (XAFS) analysis, revealing the dynamic evolution of catalytically active structures during the OER process. The Co_3O_4/MnNC nanocatalyst, identified through experimental screening and DFT optimization, exhibited low overpotentials of 296 and 401 mV at current densities of 10 and 100 mA·cm^{-2}, respectively. Long-term durability testing at 10 mA·cm^{-2} confirmed outstanding stability over 240 hours, with only a ~36 mV increases in overpotential. Overall, controlling the catalyst–support interface via single-atom metal selection is an effective route to simultaneously improve activity and durability for non-precious-metal oxygen-evolution catalysts under acidic conditions.

2 Experimental details

2.1 Chemicals

Cobaltous nitrate hexahydrate ($Co(NO_3)_2·6H_2O$, AR), Manganese(II) nitrate tetrahydrate ($Mn(NO_3)_2·4H_2O$, AR), and melamine ($C_3H_6N_6$, AR) were purchased from Aladdin. Sulfuric acid (H_2SO_4, 98%, AR) was purchased from Energy Chemical. Carbon cloth substrates were purchased from Toray TGP-H series (Japan). Nafion D-521 (5 wt.%) dispersion was purchased from Alfa Aesar. All chemicals were used without further purification.

2.2 Preparation of pure Co_3O_4

In a typical synthesis, a carbon paper (CP) sample with dimensions of 1 cm × 2.5 cm was first soaked in ethanol and then subjected to oxidation in a 0.5 M H_2SO_4 solution. Cyclic voltammetry (CV) was performed within a potential range of 1.5–2.3 V (vs. Ag/AgCl in saturated KCl) for 10 cycles. Subsequently, a portion of the oxidized CP (1 cm × 1 cm) was immersed in a 0.1 M $Co(NO_3)_2$ solution for electrodeposition of cobalt species. During the electrodeposition process, a Pt foil and an Ag/AgCl electrode (in saturated KCl solution) were employed as the counter and reference electrodes, respectively. The deposition was conducted under a constant current density of −10 mA·cm^{-2} for 50 min using a CHI 760E workstation. After electrodeposition, the sample was exposed to air to facilitate the formation of surface oxide and hydroxide layers (denoted as $Co(OH)_2$/CP). The resulting $Co(OH)_2$/CP was then annealed at 350 °C for 1 h under a nitrogen atmosphere with a heating rate of 3 °C·min^{-1}, followed by natural cooling to room temperature, to obtain the Co_3O_4 sample.

2.3 Preparation of Co_3O_4/MnNC and Co_3O_4/NC

A procedure similar to that used for synthesizing the Co_3O_4 sample was employed to prepare the $Co(OH)_2$/CP precursor. Separately, 1 g of melamine was dissolved in distilled water to form a melamine solution. Meanwhile, 148.5 mg (0.592 mmol) of manganese nitrate tetrahydrate ($Mn(NO_3)_2·4H_2O$) was dissolved in 10 mL of distilled water with stirring for 1 hour until completely dissolved. Under continuous stirring, the manganese nitrate solution was gradually added to the melamine solution at a flow rate of 0.5 mL·min^{-1}. Afterward, the mixture was stirred for an additional 2 h to ensure thorough homogenization. The prepared $Co(OH)_2$/CP was then immersed in the manganese-containing melamine solution under gentle stirring for 4 h. The resulting sample was removed, dried at room temperature, and subsequently annealed at 350 °C for 1 h under a nitrogen atmosphere at a heating rate of 3 °C·min^{-1}. Finally, the sample was allowed to cool naturally to room temperature, yielding the Co_3O_4/MnNC composite. The preparation process of Co_3O_4/NC is similar to that of Co_3O_4/MnNC, only the Mn precursor in the NC carrier needs to be removed.

2.4 Preparation of Co_3O_4/MNC with different metal sites

The synthesis procedure is consistent with that of Co_3O_4/MnNC, with the only modification being the substitution of $Mn(NO_3)_2·4H_2O$ with 0.592 mmol of the desired metal precursor.

2.5 Preparation of Co_3O_4/MnNC with different MnNC coverages

A procedure similar to that used for synthesizing the Co_3O_4 sample was employed to prepare the $Co(OH)_2$/CP precursor. The $Co(OH)_2$/CP surface was encapsulated with epoxy resin according to a predefined area ratio. Following this, melamine/Mn encapsulation was carried out in accordance with the Co_3O_4/MnNC synthesis strategy. The epoxy resin layer was then thoroughly removed using acetone. Finally, after thoroughly removing the epoxy resin layer with acetone, the resulting $Co(OH)_2$/CP was annealed following the Co_3O_4/MnNC synthesis protocol.

2.6 Preparation of MnNC

A total of 148.5 mg of $Mn(NO_3)_2·4H_2O$ was dissolved in 10 mL of distilled water with stirring for 1 h until completely dissolved. The resulting solution was gradually added to an aqueous melamine solution at a flow rate of 0.5 mL·min^{-1} under continuous stirring, followed by an additional 2 h of stirring to ensure thorough mixing. The prepared mixture was then drop-cast onto a 1 cm × 2.5 cm carbon paper substrate placed on a flat surface. To ensure uniform deposition, the mixture was added drop by drop, with the carbon paper dried at 80 °C on a hot plate between each addition. This cycle was repeated until the liquid completely evaporated. After drying, the carbon paper coated with solid material was transferred to a ceramic boat and annealed at 350 °C under a nitrogen atmosphere for 1 hour, with a heating rate of 3 °C·min^{-1}. Finally, the sample was allowed to cool naturally to room temperature, yielding MnNC.

2.7 Materials characterization

The surface composition and valence states were analyzed with X-ray photoelectron spectroscopy (XPS), using an Escalab 250Xi X-ray photoelectron spectrometer (Thermo Fisher) with Al Kα (1486.6 eV) X-rays as the excitation source, and the binding energy of the C 1 s peak at 284.8 eV was taken as an internal reference. The morphologies were examined by SEM conducted on a Hitachi SU4800 scanning electron microanalyzer with an accelerating voltage of 15 kV. The crystal phases were

characterized by powder X-ray diffraction (XRD, Rigaku D/max 2500Pc, Cu-Kα radiation, λ = 1.5406 Å). Transmission electron microscope (TEM) images were conducted on FEI Talos F200X G2 TEM equipment. High-angle annular dark-field scanning TEM (HAADF-STEM) images and energy dispersive spectra (EDS) elemental mapping were conducted on FEI Themis Z TEM equipment. The HAADF-STEM images were measured by JEOL JEM-ARM200F, which worked at an accelerating voltage of 300 kV. The metal content was monitored by inductively coupled plasma optical emission spectrometry (ICP-OES), which was carried out on Thermo Fisher IRIS Intrepid II.

2.8 Electrochemical measurements

All of the electrochemical tests were carried out at room temperature using an electrochemical station (CHI 760E, CH Instrument Co., Ltd, Shanghai, China) equipped. The Co_3O_4, MnNC or Co_3O_4/MnNC catalyst grown on carbon paper was directly used as the working electrode, along with an Ag/AgCl reference electrode and a carbon rod counter electrode in 0.5 M H_2SO_4 solution. CV was performed at the scan rate of 5 mV·s^{-1}. Electrochemical impedance spectroscopy (EIS) was collected in the frequency range from 100 kHz to 50 mHz. All CV curves were manually *iR*-corrected based on EIS results. To extract the double-layer capacitance (C_{dl}), CV was collected in pre-OER potential region at various scan rates from 10 to 120 mV·s^{-1}. All potentials used in this work have been converted to the RHE scale. All of the potentials were calibrated to the reversible hydrogen electrode according to the Nernst equation.

$$E_{RHE} = E_{(Ag/AgCl)} + 0.197 + 0.0592 \times pH \quad (1)$$

The operational stability of the catalyst was tested by running chronopotentiometry tests at a constant geometric catalytic current density of 10 mA·cm^{-2} or 100 mA·cm^{-2} in 0.5 M H_2SO_4 solution.

2.9 Analytic method

The XAFS measurement method and analytical methods can be obtained from Text S1 in the Electronic Supplementary Material (ESM). The DFT calculation method can be obtained from Text S2 in the ESM.

3 Results and discussion

3.1 Interface modulation by single-atom dopants

During the acidic OER, catalytic efficiency strongly depends on the electronic structure of surface metal sites, particularly the precise regulation of their oxidation states [38, 39]. Moreover, cobalt-based oxide catalysts often suffer from severe corrosion and dissolution, leading to the irreversible loss of active sites and significantly compromising their long-term electrochemical stability [40, 41]. Therefore, we demonstrate an interface strategy designed to simultaneously enhance both catalytic activity and stability (Fig. 1(a)). Specificly, we employed an electrochemical method to directly deposit Co_3O_4 nanocatalysts on hydrophilically treated CP substrates (Fig. S1 in the ESM). Initially, in a typical three-electrode system, Co species were uniformly nucleated and grown on the pretreated CP surface via constant-current deposition, forming a structurally homogeneous $Co(OH)_2$ precursor film. Notably, the hydrophilic pretreatment of the CP substrate played a crucial role in achieving uniform cobalt deposition. Subsequently, the obtained $Co(OH)_2$/CP composite was immersed in a precursor solution containing metal-coordinated melamine complexes. Under constant stirring at 60 °C until complete solvent evaporation, this step ensured uniform coverage of metal precursors on the $Co(OH)_2$ surface. Finally, annealing was performed under nitrogen protection, during which two critical transformations occurred simultaneously: (1) the thermal oxidation of $Co(OH)_2$ precursors into spinel-type Co_3O_4 and (2) the pyrolysis of metal-melamine complexes to form metal-anchored nitrogen-doped carbon (MNC) shells. By precisely controlling the loading amount of metal precursors, we effectively prevented metal atom agglomeration.

Systematic electrochemical measurements on cobalt oxide/nitrogen-doped carbon heterostructures with single-metal-atom coatings (M–N–C; M = Y, Ti, V, Mn, Fe, Co, Ni, Cu, Zn, Mo) reveal a trend-like dependence of acidic oxygen evolution activity on the dopant identity, with the cobalt oxide/manganese–nitrogen–carbon sample emerging as the best performer under identical preparation and testing protocols (Fig. 1(b) and Fig. S2 in the ESM). This experimentally established overpotential pattern resembles a "volcano-type" behavior (Fig. 1(c)). Guided by this observation, we interpret the trend through interfacial charge modulation at the cobalt oxide/M–N–C junction, for which electronegativity serves as a convenient screening lever to bias electron flow—useful but not definitive, since local coordination and coverage also contribute.

To rationalize the measurements, DFT was used to relate the reaction barrier to the dopant descriptor, yielding an electronegativity–barrier trend in which manganese lies near the apparent optimum (Fig. 1(d)). The intermediate electronegativity of manganese (Pauling value 1.55) is consistent with optimized adsorption free energies and a minimized rate-determining step barrier (ΔG = 1.56 eV). On this basis, manganese was selected for detailed study—not only for its high activity in testing, but also because its interfacial electronic effects provide a suitable platform for investigating how dopant choice modulates (rather than solely determines) catalytic performance. Guided by this interfacial framework—rather than electronegativity alone—we therefore selected manganese for detailed study of structure–activity relationships. For comparison, Co_3O_4 coated with N-doped carbon (Co_3O_4/NC), pure Co_3O_4, and MnNC were also prepared.

3.2 Structure characterization

The morphology of Co_3O_4/MnNC was characterized by scanning electron microscopy (SEM), revealing the nanoflower structure of the Co_3O_4 (Fig. 2(a)). Large-scale SEM images show a uniformly encapsulated N-doped C layer surrounding the Co_3O_4 core (Fig. S3 in the ESM). The phase composition and structure of various electrocatalysts were analyzed using XRD (Fig. S4 in the ESM). For Co_3O_4 and Co_3O_4/MnNC, the main diffraction peaks at 31.2°, 36.7°, 59.2°, and 65.0° correspond to the (220), (311), (511), and (440) planes of Co_3O_4 (PDF#80-1542), respectively. The XRD pattern of MnNC exhibits two diffraction peaks at 23.8° and 44.0°, corresponding to the (002) and (101) planes of carbon. No crystalline Mn signals are observed in the XRD patterns of MnNC, indicating that no Mn nanoparticles are formed. TEM confirmed the carbon-coated nanoflower structure of Co_3O_4/MnNC (Fig. 2(b)). High-resolution TEM (HRTEM) further revealed a uniform carbon capping layer with a thickness of approximately 3.50 nm surrounding the Co_3O_4 crystals (Fig. 2(c)). The measured lattice spacing of 0.25 nm is consistent with the (311) plane of

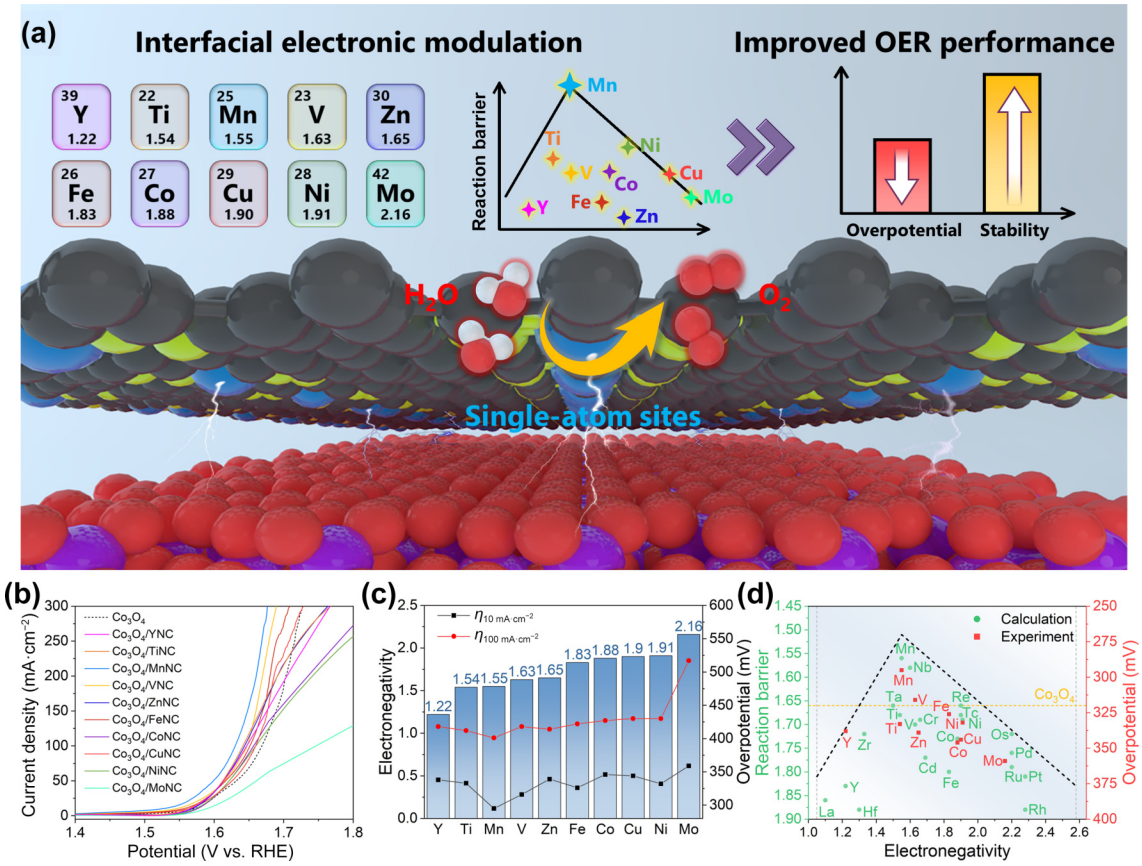

Figure 1 Scheme of an interface strategy via interfacial charge-modulation screening to enhance acidic OER and the corresponding performance and DFT results. (a) Schematic of charge modulation screening to enhance acidic OER strategy. (b) LSV curves for Co_3O_4 and Co_3O_4 with different anchored metal sites electrodes in 0.5 M H_2SO_4. (c) Overpotentials at 10 and 100 mA·cm^{-2} extracted from (b), showing a trend-like dependence on dopant identity. (d) Computed limiting reaction barrier for the acidic oxygen evolution reaction at the Co_3O_4/MNC interface; an electronegativity–barrier trend is provided as an interpretive aid rather than a deterministic descriptor.

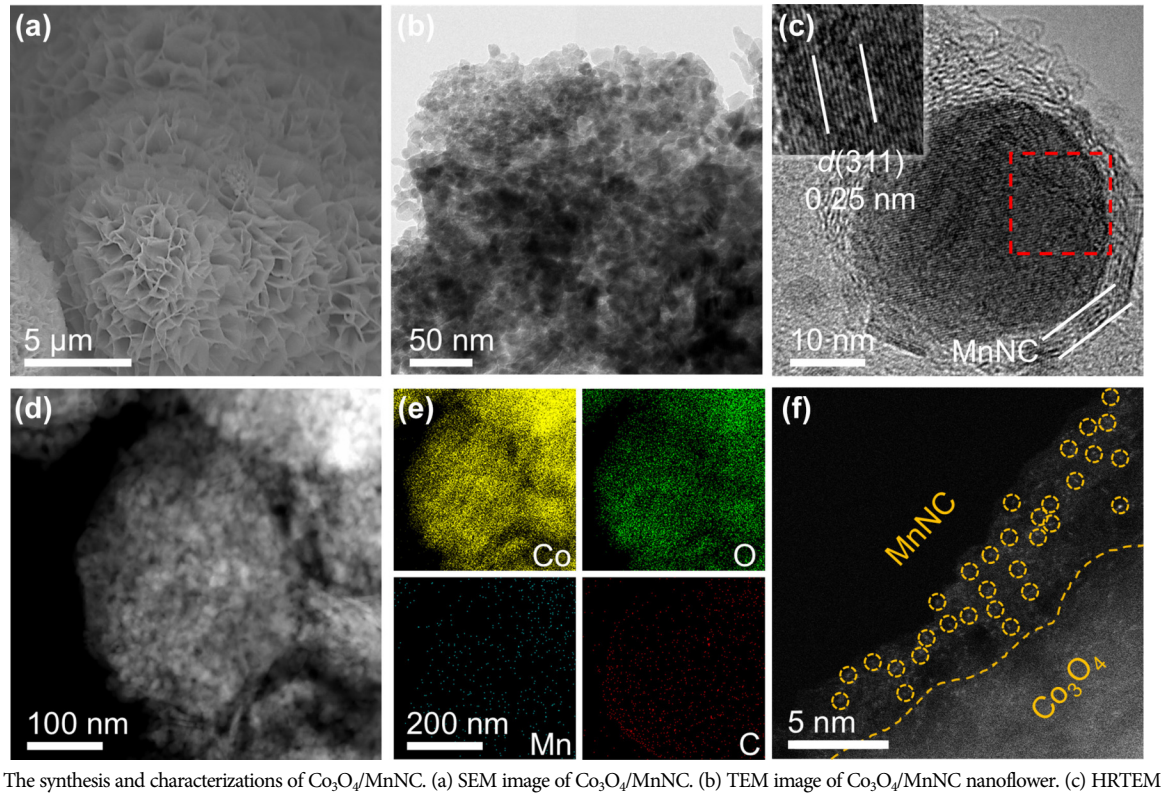

Figure 2 The synthesis and characterizations of Co_3O_4/MnNC. (a) SEM image of Co_3O_4/MnNC. (b) TEM image of Co_3O_4/MnNC nanoflower. (c) HRTEM image of Co_3O_4/MnNC to verify the encapsulated carbon layer. (Insert is enlarged HRTEM image). (d) HAADF-STEM image and (e) corresponding EDS elemental distribution mapping of Co_3O_4/MnNC, Co (yellow), O (green), Mn (blue) and C (red). (f) High-magnification HAADF-STEM image of Co_3O_4/MnNC.

Co_3O_4, in agreement with the XRD results. EDS mapping (Figs. 2(d) and 2(e)) confirmed that Co, O, Mn, N, and C elements were homogeneously distributed in the material, with negligible impurities. The successful elemental doping in selected representative Co_3O_4/MNC composites was clearly demonstrated through EDS analysis (Figs. S5–S10 in the ESM). To investigate the dispersion of Mn atoms within the nitrogen-doped carbon layer, HAADF-STEM was employed. As shown in Fig. 2(f), the Mn atoms in the MnNC cladding layer are isolated and well-dispersed. Atomically dispersed bright spots, highlighted with yellow ovals, are attributed to Mn atoms heavier than N and C. Three-dimensional Gaussian fitting mapping (Fig. S11 in the ESM) further confirmed the monodispersed nature of Mn atoms. Intensity profiles revealed that the average distance between adjacent Mn single atoms (~0.78 nm) significantly exceeds the atomic radius of Mn, verifying the atomic dispersion of Mn species. ICP-OES quantitatively determined the Mn content in Co_3O_4/MnNC and MnNC to be 1.28 wt.% and 1.35 wt.%, respectively (Table S1 in the ESM). Additionally, TEM, HAADF-STEM, and EDS mapping characterizations of Co_3O_4/NC, Co_3O_4, and MnNC were also performed (Figs. S12–S14 in the ESM).

Interfacial interactions arising from uneven charge distribution are often accompanied by charge transfer. XPS was employed to analyze the surface elemental composition and chemical states of Co_3O_4/MnNC and reference samples, confirming the presence of Mn, Co, C, N, and O (Figs. S15–S18 in the ESM). High-resolution C 1s and N 1s spectra reveal peaks characteristic of the N-doped carbon layer. In the O 1s spectrum of Co_3O_4/MnNC, three distinct peaks are observed at 531.3, 532.1, and 533.3 eV, corresponding to metal–oxygen bonds (M–O), metal–oxygen–metal bonds (M–O–M), and surface-adsorbed water (H–O–H), respectively. The high-resolution Mn 2p spectrum displays two characteristic peaks at 653.9 and 642.2 eV, attributed to Mn $2p_{1/2}$ and Mn $2p_{3/2}$, respectively (Fig. S19 in the ESM). Compared to MnNC, the Mn^0 and Mn^{x+} peaks in Co_3O_4/MnNC shift by 0.38 and 0.41 eV toward lower binding energies, indicating that charge transfer at the Co_3O_4/MnNC interface primarily occurs toward Mn. This increased electronic flow from Co_3O_4 to MnNC is likely due to the redistribution of electron density induced by the introduction of the MnNC layer, which enhancing its electron-accepting ability.

The XAFS analysis provides detailed insights into the oxidation states and local coordination environments of metal sites within the catalyst. The X-ray absorption near-edge structure (XANES) spectra at the Co K-edge indicate that the primary oxidation state of Co in all samples lies between that of Co foil and the Co_3O_4 standard, suggesting partial reduction of the synthesized Co_3O_4 relative to the standard (Fig. 3(a)). The XANES curves and corresponding valence state fittings indicated that the average oxidation states of Co in Co_3O_4/MnNC, Co_3O_4/NC, and Co_3O_4 are +2.46, +2.54, and +2.55, respectively (Fig. 3(b)). Compared

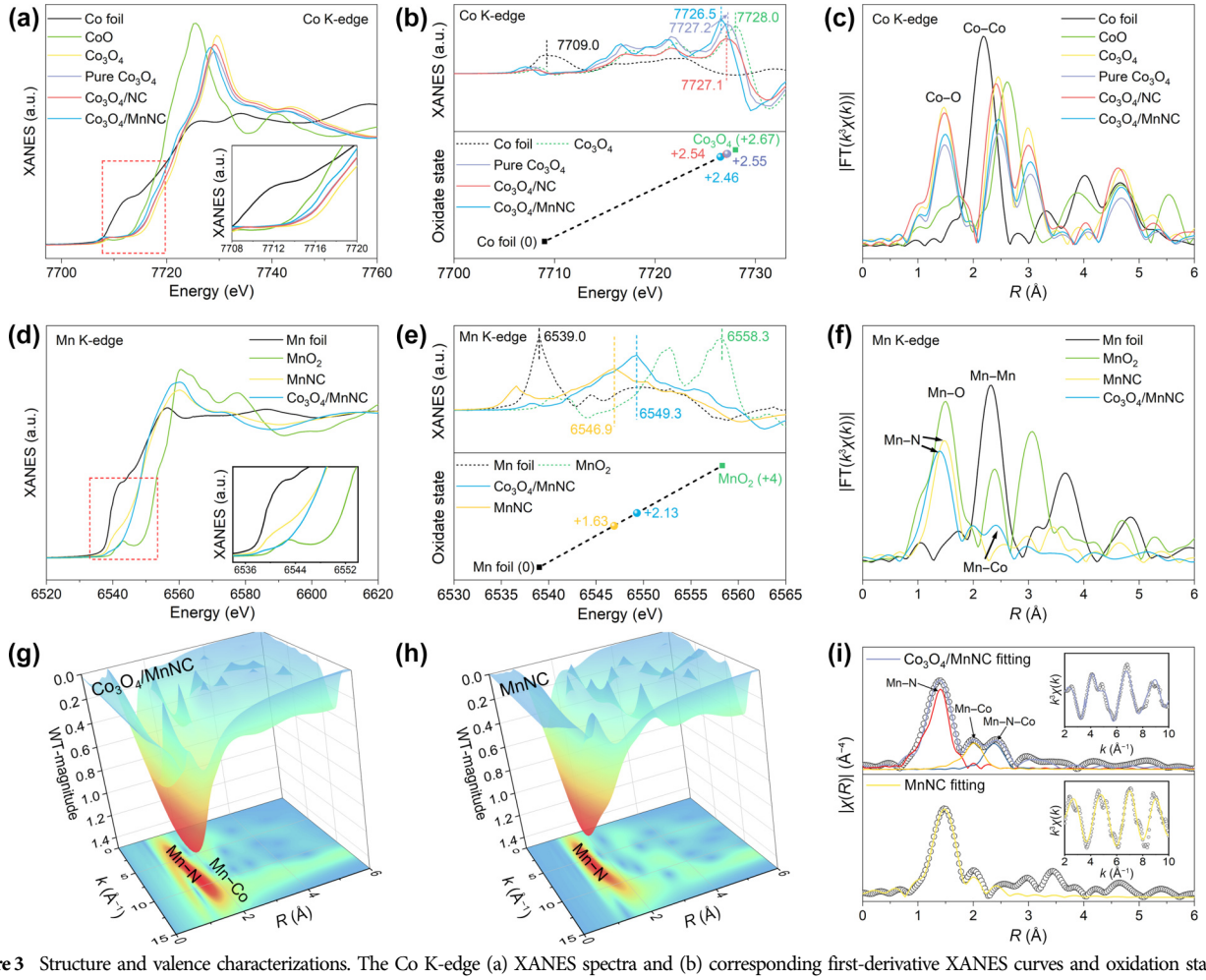

Figure 3 Structure and valence characterizations. The Co K-edge (a) XANES spectra and (b) corresponding first-derivative XANES curves and oxidation states of Co_3O_4/MnNC. (c) The EXAFS spectra of Co_3O_4/MnNC and the references at Co K-edge. The Mn K-edge (d) XANES spectra and (e) corresponding first-derivative XANES curves and oxidation states of Co_3O_4/MnNC. (f) The EXAFS spectra of Co_3O_4/MnNC and the references at Mn K-edge. WT-EXAFS images of (g) Co_3O_4/MnNC and (h) MnNC at Mn K-edge. (i) EXAFS fitting of Co_3O_4/MnNC and MnNC in *R* space at the Mn K-edge (insert is fitting curve in *k* space).

with pure Co_3O_4, the Co oxidation state variation in Co_3O_4/NC is not significant. In the Co_3O_4/MnNC sample, the pre-edge peak of Co shifts to a lower energy compared to Co_3O_4, confirming that the oxidation state of Co is mainly reduced by the introduction of Mn. The Fourier-transformed extended X-ray absorption fine structure (FT-EXAFS) spectra at the Co K-edge reveal that the Co coordination environment in both Co_3O_4/MnNC and Co_3O_4 closely resembles that of the Co_3O_4 standard, indicating structural stability (Fig. 3(c)). The Co K EXAFS spectra of Co foil displays a dominant Co–Co peak at ~2.2 Å, whereas Co_3O_4/MnNC shows Co–Co contributions at higher radial distances of ~2.4 and 3.1 Å, characteristic of the spinel lattice. These latter features can be assigned to Co_{oct}–Co_{oct} and Co_{oct}–Co_{tet} scattering paths in Co_3O_4. Relatively, the Mn K-edge XAFS spectra clearly indicate the charge transfer and structural changes occurring at the Co_3O_4/MnNC interface. Compared to MnNC, Co_3O_4/MnNC exhibits a higher absorption edge energy, reflecting an increase in the average oxidation state (Fig. 3(d)). The first-derivative XANES curve shows that the oxidation state of Mn lies between those of Mn foil and MnO_2 standards (Fig. 3(e)) [42, 43]. Based on the Mn K-edge XANES spectra, the fitted oxidation states of Mn in Co_3O_4/MnNC and MnNC are +2.13 and +1.63, respectively, consistent with the charge transfer trends observed in the XPS analysis. The valence analysis indicates interfacial charge transfer from Mn to Co in Co_3O_4/MnNC. In addition, regarding the local coordination structure of Mn, the FT-EXAFS spectrum at the Mn K-edge reveals a distinct signal peak at 1.48 Å in MnNC, corresponding to the Mn–N bond (Fig. 3(f)). The absence of significant Mn–Mn signals, as compared to Mn foil and MnO_2, confirms the formation of nitrogen-stabilized, atomically dispersed Mn. In Co_3O_4/MnNC, two prominent signal peaks at 1.44 and 2.41 Å are observed, attributed to Mn–N and Mn–Co scattering signals, respectively. The shortening of the Mn–N bond is likely due to interactions between the surface MnNC layer and the underlying metal oxide.

The wavelet transform (WT)-EXAFS at the Mn K-edge was utilized to further explore the atomic configuration of Co_3O_4/MnNC and MnNC (Figs. 3(g) and 3(h)). The WT contour plot of Co_3O_4/MnNC exhibits a peak at 5.85 $Å^{-1}$ with the highest intensity, attributed to the Mn–N bond, while a weaker Mn–Co signal is observed at 6.52 $Å^{-1}$. In contrast, MnNC exhibits a single peak at 5.83 $Å^{-1}$, corresponding to the Mn–N bond, with no evidence of metallic bonding, thereby confirming atomic dispersion [44]. The Mn K-edge EXAFS fitting results provide the true coordination information of Mn sites (Fig. 3(i)). The fitting results show excellent consistency, with the detailed results presented in Figs. S20 and S21 and Table S2 in the ESM. The first coordination shell of the central Mn atom in MnNC comprises a coordination number of 4, consisting of four N atoms with an average bond length of 1.93 Å. For Co_3O_4/MnNC, the Mn center exhibits a higher coordination number, involving four N atoms and an additional Co atom, with average bond lengths of 1.94 and 2.73 Å, respectively. Notably, the slightly elongated atomic distance between Co and Mn suggests that they are not directly bonded but instead form a Co–N–Mn interfacial structure.

3.3 Electronic structure characterization

The electrocatalytic OER performance of Co_3O_4/MnNC and reference samples was systematically evaluated under acidic conditions. The linear sweep voltammetry (LSV) curves (Fig. 4(a)) reveal that Co_3O_4/MnNC achieves the lowest overpotential, highlighting its superior catalytic activity compared to MnNC and Co_3O_4. Specifically, the reported overpotentials to attain current densities of 10 and 100 $mA·cm^{-2}$ are summarized in Fig. 4(b). Co_3O_4/MnNC exhibits overpotentials of 296 and 401 mV, respectively, which are significantly lower than those of Co_3O_4 (341 and 439 mV) and MnNC (393 and 523 mV). The performance of the Co_3O_4/MnNC catalyst surpasses that of other OER electrocatalysts, as demonstrated in Fig. 4(c) and Table S3 in the ESM. The Tafel slopes derived from the polarization curves (Fig. S22 in the ESM) further demonstrate differences in reaction kinetics. Co_3O_4/MnNC displays the smallest Tafel slope of 73.7 $mV·dec^{-1}$, indicating a more efficient charge transfer process compared to Co_3O_4 (95.7 $mV·dec^{-1}$), MnNC (104.9 $mV·dec^{-1}$) and com-RuO_2 (82.8 $mV·dec^{-1}$). EIS measurements were conducted to evaluate the charge transfer resistance (R_{ct}) of the samples. The Nyquist plots (Fig. S23 in the ESM) show that Co_3O_4/MnNC exhibits the lowest R_{ct} value, reflecting faster electron transfer kinetics during the OER process. This result aligns with its superior performance in LSV and Tafel analyses. The electrochemically active surface area (ECSA) is estimated from the electrochemical double-layer capacitance (Fig. S24 in the ESM). As depicted in Fig. S25 in the ESM, Co_3O_4/MnNC has the highest C_{dl} value of 31.95 $mF·cm^{-2}$, indicating a larger ECSA and a higher density of active sites compared to Co_3O_4 (19.36 $mF·cm^{-2}$) and MnNC (20.03 $mF·cm^{-2}$). To directly investigate the role of the Co–N–Mn interfacial structure in catalytic performance, a series of Co_3O_4/MnNC electrodes with controlled MnNC coverage (0%, 25%, 50%, 75%, and 100%) were fabricated (Fig. 4(d)), following the method described in the synthesis section. The overpotentials for 10 and 100 $mA·cm^{-2}$ decrease gradually with increasing interface coverage (Figs. 4(f) and 4(e)). The linear correlation between the overpotentials and the coverages confirms that the Co-N-Mn interface as active site is responsible for the enhancement of the performance.

The durability of the Co_3O_4/MnNC catalyst in acidic media is a critical parameter for practical applications. Figure 4(g) illustrates the chronoamperometric potential responses of the Co_3O_4/MnNC catalyst under constant OER current densities of 10 and 100 $mA·cm^{-2}$. At 10 $mA·cm^{-2}$, the Co_3O_4/MnNC catalyst demonstrates a relatively stable overpotential, increasing from 292 to 328 mV over 240 h of continuous operation. Even at a higher current density of 100 $mA·cm^{-2}$, the catalyst maintains operational stability for more than 100 h, with only a slight increase in overpotential from 424 to 442 mV. In contrast, Co_3O_4 without MnNC protection exhibits severe degradation in stability, likely due to the dissolution of Co_3O_4 under acidic electrolyte. Post-stability testing LSV measurements (Fig. 4(h)) indicate minimal loss in catalytic activity, confirming the durability of Co_3O_4/MnNC under harsh electrochemical conditions. Structural and morphological analyses further corroborate the catalyst's robustness. HRTEM and HAADF-STEM images confirm that Co_3O_4/MnNC retains its initial MnNC core-shell structure, with Mn atoms in MnNC maintaining their atomically dispersed characteristics (Fig. S26 in the ESM).

Moreover, the EXAFS spectra and their corresponding fitting curves further reveal that the coordination structure of MnNC remains largely unchanged compared to the pre-reaction sample, with no significant structural alterations (Fig. S27 in the ESM). Collectively, these findings underscore the outstanding stability and structural integrity of the Co_3O_4/MnNC catalyst, reinforcing its potential as a highly durable electrocatalyst for acidic OER.

3.4 *In situ* XAFS test and analysis

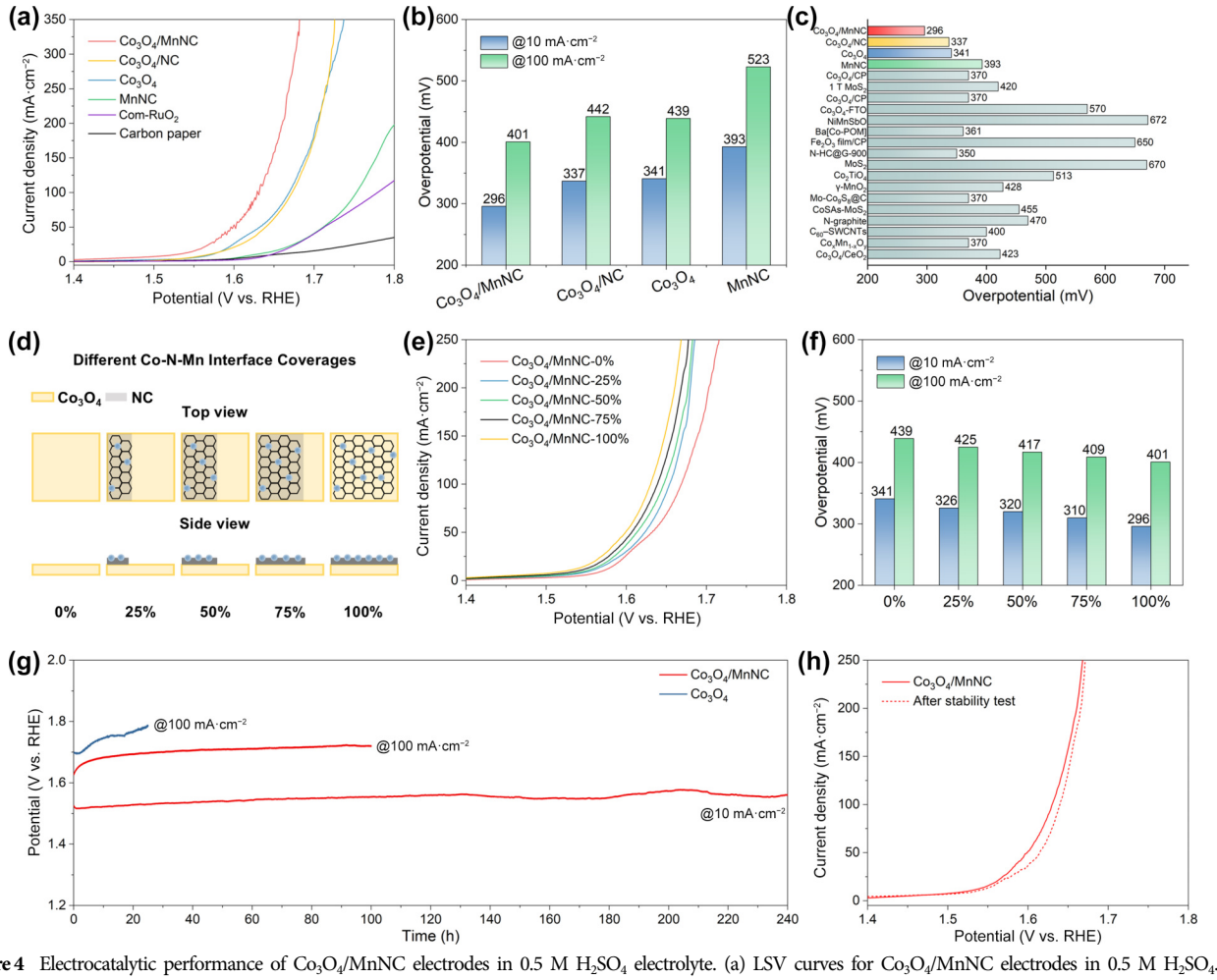

Figure 4 Electrocatalytic performance of Co_3O_4/MnNC electrodes in 0.5 M H_2SO_4 electrolyte. (a) LSV curves for Co_3O_4/MnNC electrodes in 0.5 M H_2SO_4. (b) Overpotential statistics of Co_3O_4/MnNC, Co_3O_4 and MnNC at various current densities. (c) Comparison of OER performance of various electrocatalysts. (d) Model plots for different Co-N-Mn interface coverages. (e) LSV curves for Co_3O_4 with different degrees of MnNC coverage in 0.5 M H_2SO_4. (f) Overpotential statistics of Co_3O_4 with different degrees of MnNC coverage. (g) Chronopotentiometric response of the Co_3O_4/MnNC catalyst in an H-type cell at 10 and 100 mA·cm^{-2}. (h) LSV curves before and after stability testing.

To gain insight into the structure evolution of the catalysts during the OER process, *in situ* XAFS measurements were performed on Co_3O_4/MnNC, Co_3O_4 and MnNC materials under various conditions: *ex situ*, open circuit potential (OCP), 1.4, and 1.6 V (vs. RHE) [45–47]. The charge transfer dynamics at the Co–N–Mn interface are effectively demonstrated by the valence state changes observed at the Co and Mn K-edges under *in situ* conditions. In the Mn K-edge XANES spectra of Co_3O_4/MnNC, a clear and progressive shift toward higher energies is observed with increasing applied potential, indicating a gradual increase in the oxidation state of Mn during OER (Figs. 5(a) and 5(b)). Although a similar trend was observed for MnNC, the magnitude of the shift is significantly less pronounced (Figs. 5(c) and 5(d)). This observation suggests enhanced redox responsiveness of Mn in the Co_3O_4/MnNC composite, attributable to the interfacial electronic interactions with Co. To quantitatively assess the redox behavior, the first-derivative XANES curves were employed to determine the Mn oxidation states at different potentials. For Co_3O_4/MnNC, the Mn oxidation states at the respective potentials were as follows: 1.91 (*ex situ*), 2.05 (OCP), 2.18 (1.4 V), and 2.26 (1.6 V) (Fig. 5(e)). In contrast, MnNC exhibits only minor changes in Mn oxidation state: 2.49 (*ex situ*), 2.54 (OCP), 2.57 (1.4 V), and 2.60 (1.6 V), which showed much smaller changes compared to Co_3O_4/MnNC (Fig. 5(f)). The extent of Mn oxidation in MnNC was less pronounced compared to Co_3O_4/MnNC, indicating that the presence of Co in the composite enhances the dynamic redox activity of Mn under OER conditions. In addition, the Mn valence state in Co_3O_4/MnNC remains consistently higher than that in MnNC throughout the reaction, indicating a strong interfacial interaction between Co_3O_4 and MnNC that facilitates charge transfer from Mn to Co.

The Co K-edge XANES spectra reveal that the Co species in both Co_3O_4/MnNC and pristine Co_3O_4 exhibit increased valence states under oxidative potentials (Figs. 5(g) and 5(h)). However, valence changes resulting from atomic interactions in Co_3O_4 are not significant, owing to the high proportion of Co atoms. Notably, the Co K-edge in Co_3O_4 appears at a slightly lower energy relative to that in Co_3O_4/MnNC (Figs. 5(i) and 5(j)), implying that electron donation from Mn in the MnNC shell to the Co_3O_4 core results in a reduced average Co valence state. This interfacial electron transfer effect becomes more apparent in the quantitative oxidation state fitting results. For Co_3O_4/MnNC, the fitted Co oxidation states progressively increase from 1.76 (*ex situ*) to 1.80 (OCP), 1.83 (1.4 V), and 1.88 (1.6 V) (Fig. 5(k)). In contrast, the corresponding oxidation states for pristine Co_3O_4 are significantly higher and show minimal variation: 2.60 (*ex situ*), 2.66 (OCP), 2.67 (1.4 V), and 2.68 (1.6 V) (Fig. 5(l)). The pronounced changes in oxidation states observed for

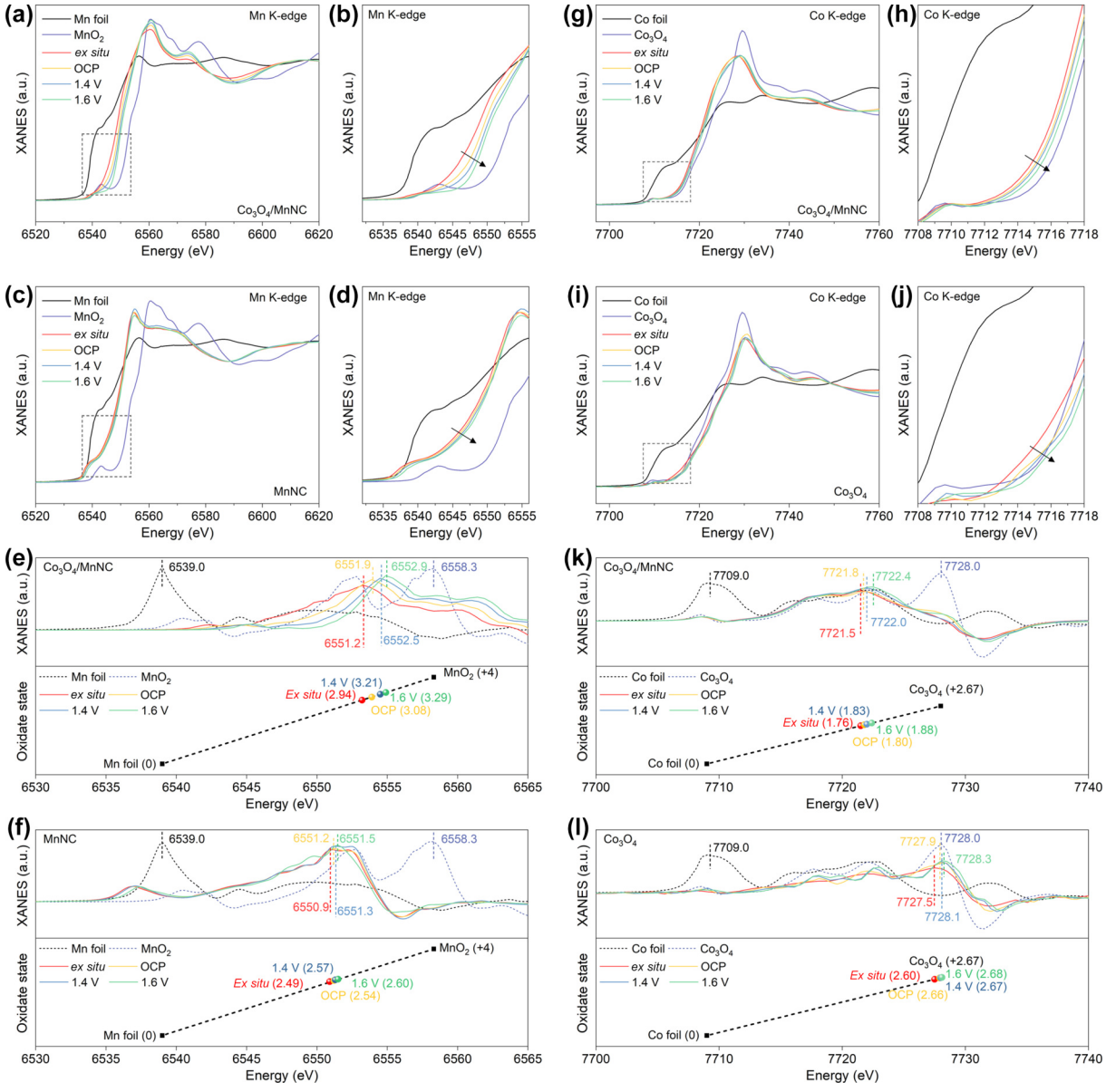

Figure 5 *In situ* XAFS characterizations of Co_3O_4/MnNC. (a) *In situ* Mn K-edge XANES spectra and (b) corresponding magnified spectra of Co_3O_4/MnNC during electrochemical OER. (c) *In situ* Mn K-edge XANES spectra and (d) corresponding magnified spectra of MnNC. First-derivative XANES curves and corresponding oxidation states of (e) Co_3O_4/MnNC and (f) MnNC at the Mn K-edge. (g) *In situ* Co K-edge XANES spectra and (h) corresponding magnified spectra of Co_3O_4/MnNC during electrochemical OER. (i) *In situ* Co K-edge XANES spectra and (j) corresponding magnified spectra of Co_3O_4. First-derivative XANES curves and corresponding oxidation states of (k) Co_3O_4/MnNC and (l) Co_3O_4 at the Co K-edge.

Co_3O_4/MnNC during the OER process can be attributed to significant charge transfer between the Co and Mn species. This charge transfer is attributed to a synergistic interaction at the Co–N–Mn interface, which becomes more prominent during the reaction.

The *in situ* FT-EXAFS spectra of the Co and Mn K-edge provide crucial insights into the structural evolution of Co_3O_4/MnNC under OER process. At the Co K-edge, the EXAFS spectra consistently exhibit features corresponding to Co–O and Co–Co coordination across all applied potentials (Fig. S29 in the ESM), indicating that the local Co environment remains structurally stable throughout the reaction. The Mn K-edge EXAFS fitting results reveal that the Co–N–Mn coordination remains stable with increasing reaction potential, indicating that the interfacial Co–N–Mn structure is robust and well-preserved under OER operating conditions (Fig. S30 and Tables S4 and S5 in the ESM). The Co–N–M structure not only boosts catalytic activity but also suppresses structural relaxation, thus improving the structural stability.

3.5 DFT calculations

To further gain insights into the enhanced OER activity of Co_3O_4/MnNC induced by the Co–N–Mn interface, DFT calculations were performed. The detailed computational procedures were provided in the ESM. The optimized models include Co_3O_4, MnNC, Co_3O_4/NC, and Co_3O_4/MnNC (Fig. S31 in the ESM). To investigate the intrinsic mechanism driving charge redistribution at the Co–N–Mn interface, the work functions of Co_3O_4, MnNC, and Co_3O_4/MnNC were calculated (Fig. 6(a)). The work function, defined as the minimum energy required for an electron to move from the interior of a solid to its surface, serves as a measure of electron transfer within the material. The work

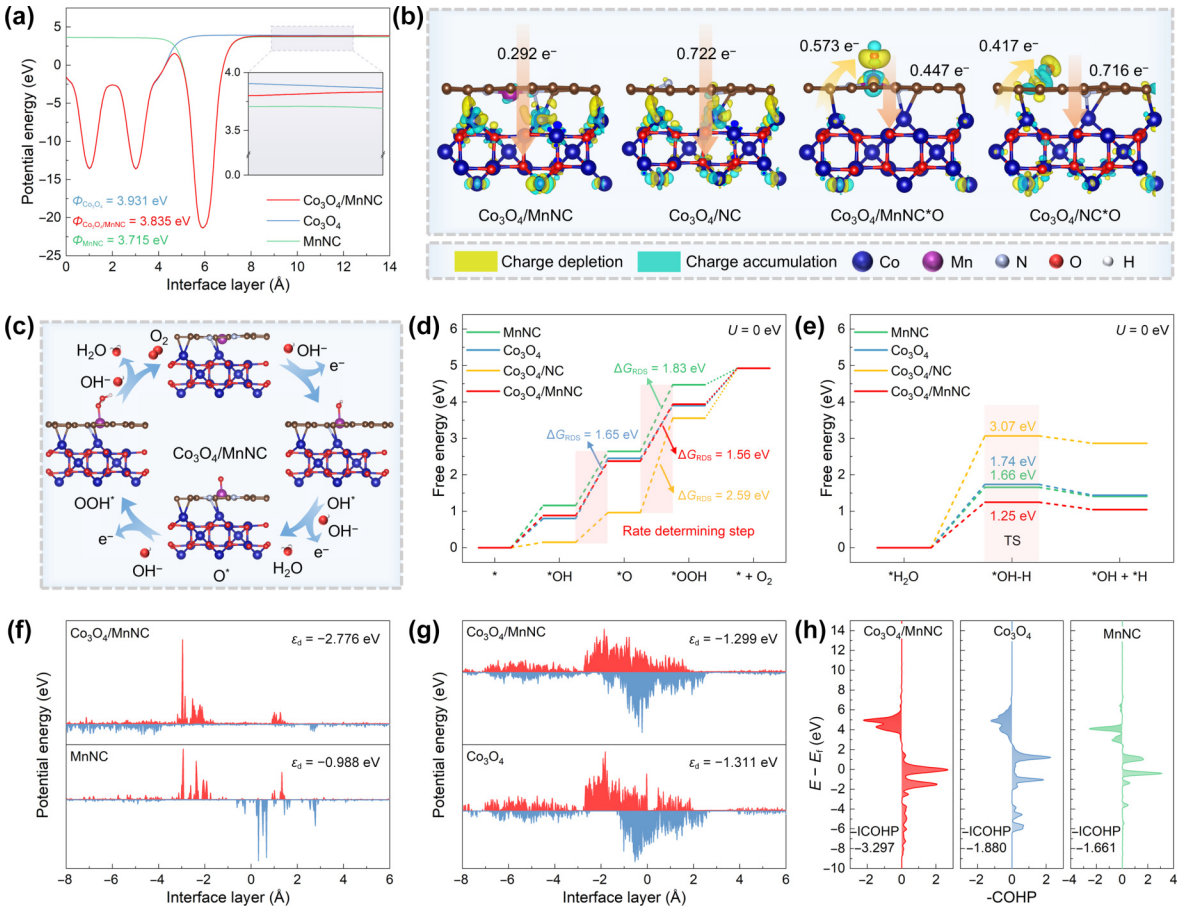

Figure 6 Theoretical OER activity of Co_3O_4/MnNC. (a) Calculated work function of Co_3O_4/MnNC, Co_3O_4 and MnNC. (b) The difference charge density at the Co_3O_4/MnNC and Co_3O_4/NC interfaces. (c) Typical OER mechanism of the Co_3O_4/MnNC catalyst. (d) Calculated free energy profiles of the Co_3O_4/MnNC, Co_3O_4/NC, Co_3O_4, and MnNC catalysts for the OER pathway, respectively. (e) Transition states of water decomposition for Co_3O_4/MnNC, Co_3O_4/NC, Co_3O_4, and MnNC catalysts. (f) Projected density of states (DOS) of Mn for Co_3O_4/MnNC and MnNC. (g) Projected DOS of Co for Co_3O_4/MnNC and MnNC. (h) The −ICOHP of Co_3O_4/MnNC, Co_3O_4 and MnNC.

function of Co_3O_4 (3.931 eV) is larger than that of MnNC (3.715 eV), indicating that electrons in MnNC are more readily able to escape from the surface to facilitate transfer. Therefore, a natural tendency for electrons to transfer from MnNC to Co_3O_4. The charge density differences between Co_3O_4/MnNC and Co_3O_4/NC quantitatively reveal the electron transfer behavior from MnNC to Co_3O_4. For Co_3O_4/MnNC, the charge transfer at the Co–N–Mn interface is 0.292e⁻, while Co_3O_4/NC exhibits lower electron transfer (Fig. 6(b)). This limitation in charge transfer persists even when both samples are adsorbed with *O, as the interfacial charge transfer in Co_3O_4/MnNC is 0.573e⁻, compared to 0.716e⁻ in Co_3O_4/NC. However, this charge transfer limitation does not extend to the overall charge transfer from Co_3O_4 to the adsorbed substrate. Co_3O_4/MnNC exhibits higher total charge transfer to the adsorbed *O at the Co–N–Mn interface. The significant charge density redistribution in Co_3O_4/MnNC highlights enhanced Co–N–Mn interfacial interactions between the MnNC shell and the Co_3O_4 core, a phenomenon that persists throughout the reaction process and aligns with the findings from XAFS and *in situ* XAFS analyses. This targeted electron transfer at the Co–N–Mn interface increases the oxidation state of Mn atoms in the shell, which serve as active sites. These higher oxidation states have been confirmed to correlate strongly with superior OER performance [48–50].

The typical OER mechanism for Co_3O_4/MnNC is illustrated in Fig. 6(c). The Gibbs free energy evolution steps for the acidic OER pathway of Co_3O_4/MnNC and reference samples are shown in Fig. 6(d). The MnNC shell acts as an "armor," preventing direct adsorption of intermediates on the internal Co_3O_4 [51–53]. Instead, the substrate preferentially adsorbs onto the Mn sites in the MnNC shell. The synergistic regulation of intermediates by Co_3O_4 and MnNC occurs through charge transfer at the interface. For Co_3O_4, the conversion of *OH to *O constitutes the RDS of the OER process due to a high reaction energy barrier of 1.65 eV. In contrast, for the other samples, the transformation from *O to *OOH serves as the primary RDS. Co_3O_4/MnNC exhibits the lowest reaction energy barrier (1.56 eV), highlighting that the precise construction of the Co–N–Mn interface significantly improves the catalytic pathway for acidic OER, outperforming MnNC (1.83 eV) and Co_3O_4/NC (2.59 eV). The efficient construction and interfacial growth under *in situ* conditions lead to a substantial reduction in overall free energy during the reaction. This reduction is attributed to the high OER activity induced by interfacial modulation and the asymmetric charge distribution caused by interfacial electron transfer, which optimizes the adsorption of key oxygen-containing intermediates. Furthermore, during the adsorption of reaction intermediates, the bond lengths of Co-N and Mn-N remained largely unchanged, consistent with the *in situ* XAFS results. To further investigate the source of the superior performance of the Co–N–Mn interface in the OER process, the water decomposition transition states of various samples were calculated to determine the initial driving

force of the reaction (Fig. 6(e)). The results indicate that Co_3O_4/MnNC, with its Co–N–Mn interface, has the lowest reaction barrier, requiring a lower overpotential for the initial water decomposition to produce *OH. Furthermore, Co_3O_4/MnNC demonstrates higher *OH coverage at the same overpotential, providing a strong driving force for subsequent adsorption and OER processes.

The charge rearrangement at the interface modifies the electronic structure of the adjacent Mn sites, which contributes to the significant enhancement of OER activity compared to Co_3O_4 and MnNC. According to the calculated DOS, the Co_3O_4/MnNC composite exhibits more favorable Fermi energy level positions and superior electrical conductivity compared to Co_3O_4 and MnNC (Figs. 6(f) and 6(g)) [54]. For Co_3O_4/MnNC, both the 3d orbitals of Mn atoms (shifted from ε_d = −2.776 to −0.988 eV) and the 3d orbitals of Co atoms (shifted from ε_d = −1.299 to −1.311 eV) are displaced relative to the Fermi level due to the interface regulation effect. The modulation of the Mn site 3d orbitals away from the Fermi level enhances the spin capacity of the electrons. Furthermore, the magnetic properties of the Mn sites are strengthened by the interfacial modulation, resulting in an asymmetric orientation of the spin electrons. This, in turn, improves the overall hydrolysis ability of the catalyst. In contrast, nitrogen in Co_3O_4/NC, which serves as the primary adsorption site, cannot act as a hydrolysis site, leading to its poor OER activity (Fig. S32 in the ESM). The Integral Crystal Orbital Hamiltonian (ICOHP) quantifies the strength of adsorption between the active site and the adsorbate. As shown in Fig. 6(h), the ICOHP values of Co_3O_4/MnNC, Co_3O_4, and MnNC are 3.297, 1.880, and 1.661, respectively. The ICOHP values reflect the contributions of bonding and antibonding states, with higher values indicating stronger binding energies. This result enhances the adsorption capacity and activation ability of Co_3O_4/MnNC toward the substrate, leading to higher reactivity during acidic OER. The Mn with more moderate electronegativity can effectively regulate the charge distribution at the interface, resulting in a better synergy between Co_3O_4 and MnNC. Therefore, Mn exhibits the lowest reaction energy barrier as the active site, which is favorable for acidic OER.

4 Conclusion

In conclusion, we advance an interfacial modulation strategy on cobalt oxide by coating it with a single-metal-atom, nitrogen-doped carbon layer. Guided by combined DFT and experiments, the cobalt oxide/manganese–nitrogen–carbon catalyst exhibits excellent activity and durability. Correlating electrochemical performance with coating coverage, together with valence-state and structural analyses, identifies the Co–N–M interface as the key motif for improving both kinetics and stability. Finally, *in situ* XAFS and DFT resolve the active Co–N–Mn interfacial structure and track its *operando* evolution, directly linking interface tuning to catalytic function. Together, these results outline a practical, generalizable route to design high-efficiency, durable oxygen-evolution nanocatalysts in acidic media by controlling the catalyst–support interface.

Acknowledgements

This work was financially supported by the National Natural Science Foundation of China (Grant 22478030). The authors thank the BL14W1 in the Shanghai Synchrotron Radiation Facility (SSRF) for help with characterizations.

Declaration of competing interest

The authors declare no conflicting interests regarding the content of this article.

Data availability

All data needed to support the conclusions in the paper are presented in the manuscript and/or the Supplementary Materials. Additional data related to this paper may be requested from the corresponding author upon request.

References

[1] Zhang, J. H.; Fu, X. B.; Kwon, S.; Chen, K. F.; Liu, X. Z.; Yang, J.; Sun, H. R.; Wang, Y. C.; Uchiyama, T.; Uchimoto, Y. et al. Tantalum-stabilized ruthenium oxide electrocatalysts for industrial water electrolysis. *Science* **2025**, *387*, 48–55.

[2] Li, L. G.; Wang, P. T.; Shao, Q.; Huang, X. Q. Metallic nanostructures with low dimensionality for electrochemical water splitting. *Chem. Soc. Rev.* **2020**, *49*, 3072–3106.

[3] Turner, J. A. Sustainable hydrogen production. *Science* **2004**, *305*, 972–974.

[4] Chong, L. N.; Gao, G. P.; Wen, J. G.; Li, H. X.; Xu, H. P.; Green, Z.; Sugar, J. D.; Kropf, A. J.; Xu, W. Q.; Lin, X. M. et al. La- and Mn-doped cobalt spinel oxygen evolution catalyst for proton exchange membrane electrolysis. *Science* **2023**, *380*, 609–616.

[5] Seitz, L. C.; Dickens, C. F.; Nishio, K.; Hikita, Y.; Montoya, J.; Doyle, A.; Kirk, C.; Vojvodic, A.; Hwang, H. Y.; Norskov, J. K. et al. A highly active and stable IrO_x/$SrIrO_3$ catalyst for the oxygen evolution reaction. *Science* **2016**, *353*, 1011–1014.

[6] An, L.; Wei, C.; Lu, M.; Liu, H. W.; Chen, Y. B.; Scherer, G. G.; Fisher, A. C.; Xi, P. X.; Xu, Z. J.; Yan, C. H. Recent development of oxygen evolution electrocatalysts in acidic environment. *Adv. Mater.* **2021**, *33*, 2006328.

[7] Zhang, B.; Zheng, X. L.; Voznyy, O.; Comin, R.; Bajdich, M.; García-Melchor, M.; Han, L. L.; Xu, J. X.; Liu, M.; Zheng, L. R. et al. Homogeneously dispersed multimetal oxygen-evolving catalysts. *Science* **2016**, *352*, 333–337.

[8] Feng, S. W.; Fan, S. Y.; Li, L.; Sun, Z. Y.; Tang, H. W.; Xu, Y.; Fang, L.; Wang, C. J. Using hollow dodecahedral NiCo-LDH with multi-active sites to modify $BiVO_4$ photoanode facilitates the photoelectrochemical water splitting performance. *Nano Res. Energy* **2024**, *3*, e9120117.

[9] Rong, C. L.; Dastafkan, K.; Wang, Y.; Zhao, C. Breaking the activity and stability bottlenecks of electrocatalysts for oxygen evolution reactions in acids. *Adv. Mater.* **2023**, *35*, 2211884.

[10] Blasco-Ahicart, M.; Soriano-López, J.; Carbó, J. J.; Poblet, J. M.; Galan-Mascaros, J. R. Polyoxometalate electrocatalysts based on earth-abundant metals for efficient water oxidation in acidic media. *Nat. Chem.* **2018**, *10*, 24–30.

[11] Simondson, D.; Tesch, M. F.; Spanos, I.; Jones, T. E.; Guo, J. N.; Kerr, B. V.; Chatti, M.; Bonke, S. A.; Golnak, R.; Johannessen, B. et al. Decoupling the catalytic and degradation mechanisms of cobalt active sites during acidic water oxidation. *Nat. Energy* **2025**, *10*, 1013–1024.

[12] Li, S. L.; Zhang, J. Q.; Li, Y. N.; Fan, P. X.; Wu, M. B. Revisiting N, S co-doped carbon materials with boosted electrochemical performance in sodium-ion capacitors: The manipulation of internal electric field. *Nano Res. Energy* **2024**, *3*, e9120098.

[13] Wang, Y. B.; Jiang, J. D.; Shi, Z. P.; Wu, H. X.; Yang, J. H.; Wang, P. B.; Hou, S.; Xiao, M. L.; Ge, J. J.; Liu, C. P. et al. Stabilizing high-efficiency iridium single atoms via lattice confinement for acidic oxygen evolution. *Nano Res.* **2024**, *17*, 2492–2498.

[14] Zhong, X.; Xu, J. Y.; Chen, J. N.; Wang, X. Y.; Zhu, Q.; Zeng, H.; Zhang, Y. W.; Pu, Y. H.; Hou, X. Y.; Wu, X. F. et al. Spatially and temporally resolved dynamic response of Co-based composite

interface during the oxygen evolution reaction. *J. Am. Chem. Soc.* **2024**, *146*, 7467–7479.
[15] Zhang, M. ; de Respinis, M.; Frei, H. Time-resolved observations of water oxidation intermediates on a cobalt oxide nanoparticle catalyst. *Nat. Chem.* **2014**, *6*, 362–367.
[16] Priamushko, T.; Franz, E.; Logar, A.; Bijelić, L.; Guggenberger, P.; Escalera-López, D.; Zlatar, M.; Libuda, J.; Kleitz, F.; Hodnik, N. et al. Be aware of transient dissolution processes in Co_3O_4 acidic oxygen evolution reaction electrocatalysts. *J. Am. Chem. Soc.* **2025**, *147*, 3517–3528.
[17] Zhou, J.; Zhang, L. J.; Huang, Y. C.; Dong, C. L.; Lin, H. J.; Chen, C. T.; Tjeng, L. H.; Hu, Z. W. Voltage- and time-dependent valence state transition in cobalt oxide catalysts during the oxygen evolution reaction. *Nat. Commun.* **2020**, *11*, 1984.
[18] Wan, R. D.; Yuan, T. H.; Wang, L. C.; Li, B.; Liu, M. L.; Zhao, B. T. Earth-abundant electrocatalysts for acidic oxygen evolution. *Nat. Catal.* **2024**, *7*, 1288–1304.
[19] Zhao, L.; Meng, K. X.; Guo, Y. B.; Wu, Q. S.; Zhu, Q. J.; Zhou, T.; Fu, Y. Q.; Wen, M. FeCoP sub-nanometric-sheets for electrocatalzing overall water splitting. *Nano Res. Energy* **2024**, *3*, e9120129.
[20] Wang, Q. L.; Cheng, Y. Q.; Tao, H. B.; Liu, Y. H.; Ma, X. H.; Li, D. S.; Yang, H. B.; Liu, B. Long-term stability challenges and opportunities in acidic oxygen evolution electrocatalysis. *Angew. Chem., Int. Ed.* **2023**, *62*, e202216645.
[21] Du, Y. B.; Liu, J. Q.; Chen, J. Y.; Wang, S. B.; Tang, Y. W.; Wang, A. L.; Fu, G. T.; Lu, X. F. Design principle and regulation strategy of noble metal-based materials for practical proton exchange membrane water electrolyzer. *Adv. Energy Mater.* **2025**, *15*, 2404113.
[22] Zhan, Z. H.; Wei, Z. H.; Zhang, Z. T.; Wang, L. P.; Cheong, W. C.; Li, S. H.; Chen, W. X.; Pang, S. P. Precisely designing atomically dispersed catalysts for C–N coupling reactions. *Nano Res. Energy* **2025**, *4*, e9120197.
[23] Wang, Y.; Guo, P.; Zhou, J.; Bai, B.; Li, Y. F.; Li, M. R.; Das, P.; Wu, X. H.; Zhang, L. J.; Cui, Y. et al. Tuning the Co pre-oxidation process of Co_3O_4 via geometrically reconstructed F–Co–O active sites for boosting acidic water oxidation. *Energy Environ. Sci.* **2024**, *17*, 8820–8828.
[24] Wang, C. M.; Geng, Q. H.; Fan, L. L.; Li, J. X.; Ma, L.; Li, C. L. Phase engineering oriented defect-rich amorphous/crystalline RuO_2 nanoporous particles for boosting oxygen evolution reaction in acid media. *Nano Res. Energy* **2023**, *2*, e9120070.
[25] Huang, Y.; Zhang, S. L.; Lu, X. F.; Wu, Z. P.; Luan, D. Y.; Lou, X. W. Trimetallic spinel $NiCo_{2-x}Fe_xO_4$ nanoboxes for highly efficient electrocatalytic oxygen evolution. *Angew. Chem., Int. Ed.* **2021**, *60*, 11841–11846.
[26] Yang, Y. F.; Xu, Y. H.; Liu, H. Q.; Zhang, Q.; Liu, B. L.; Yang, M. H.; Dai, H.; Ke, Z. J.; He, D.; Feng, X. B. et al. Unraveling the modulation essence of p bands in Co-based oxide stability on acidic oxygen evolution reaction. *Nano Res.* **2024**, *17*, 5922–5929.
[27] Wang, J.; Kim, S. J.; Liu, J. P.; Gao, Y.; Choi, S.; Han, J.; Shin, H.; Jo, S.; Kim, J.; Ciucci, F. et al. Redirecting dynamic surface restructuring of a layered transition metal oxide catalyst for superior water oxidation. *Nat. Catal.* **2021**, *4*, 212–222.
[28] Yu, J. H.; Garcés-Pineda, F. A.; González-Cobos, J.; Peña-Díaz, M.; Rogero, C.; Giménez, S.; Spadaro, M. C.; Arbiol, J.; Barja, S.; Galán-Mascarós, J. R. Sustainable oxygen evolution electrocatalysis in aqueous 1 M H_2SO_4 with earth abundant nanostructured Co_3O_4. *Nat. Commun.* **2022**, *13*, 4341.
[29] Rong, C. L.; Wang, S. H.; Shen, X.; Jia, C.; Sun, Q.; Zhang, Q.; Zhao, C. Defect-balanced active and stable Co_3O_{4-x} for proton exchange membrane water electrolysis at ampere-level current density. *Energy Environ. Sci.* **2024**, *17*, 4196–4204.
[30] Shi, X. Z.; Deng, R. R.; Zhang, Q. B. Electrochemically assisted preparation of defect-rich Co_3O_4 electrocatalysts in a water-modified deep eutectic solvent for enhanced oxygen evolution in acid. *Appl. Surf. Sci.* **2025**, *682*, 161761.
[31] Huang, J. Z.; Sheng, H. Y.; Ross, R. D.; Han, J. C.; Wang, X. J.; Song, B.; Jin, S. Modifying redox properties and local bonding of Co_3O_4 by CeO_2 enhances oxygen evolution catalysis in acid. *Nat. Commun.* **2021**, *12*, 3036.
[32] Zhou, X. Y.; Yang, T. T.; Li, T.; Zi, Y. J.; Zhang, S. J.; Yang, L.; Liu, Y. K.; Yang, J.; Tang, J. J. *In-situ* fabrication of carbon compound NiFeMo–P anchored on nickel foam as bi-functional catalyst for boosting overall water splitting. *Nano Res. Energy* **2023**, *2*, e9120086.
[33] Hartnett, A. C.; Evenson, R. J.; Thorarinsdottir, A. E.; Veroneau, S. S.; Nocera, D. G. Lanthanum-promoted electrocatalyst for the oxygen evolution reaction: Unique catalyst or oxide deconstruction. *J. Am. Chem. Soc.* **2025**, *147*, 1123–1133.
[34] Liu, K. Y.; Wang, L. P.; Chen, W. X.; Sun, Z. Y.; Geng, H. L.; Li, Y. Q.; Deng, Z. W.; Jiang, S.; Zhou, B. R.; Yu, K. D. et al. The roadmap of carbon-based single-atom catalysts: Rational design and electrochemical applications. *Rare Met.* **2025**, *44*, 7987–8132.
[35] Qiao, B. T.; Wang, A. Q.; Yang, X. F.; Allard, L. F.; Jiang, Z.; Cui, Y. T.; Liu, J. Y.; Li, J.; Zhang, T. Single-atom catalysis of CO oxidation using Pt_1/FeO_x. *Nat. Chem.* **2011**, *3*, 634–641.
[36] Nasrullah, A. R.; Zhou, Z. H.; Rehman, A.; Hussain, M.; Zheng, X. B.; Yang, Y. A.; Wang, L. G. Advances of earth-abundant cobalt-based single-atom catalysts for acidic oxygen evolution by electrolysis. *Nano Res.* **2025**, *18*, 94907593.
[37] Huang, J. Z.; Borca, C. N.; Huthwelker, T.; Yüzbasi, N. S.; Baster, D.; El Kazzi, M.; Schneider, C. W.; Schmidt, T. J.; Fabbri, E. Surface oxidation/spin state determines oxygen evolution reaction activity of cobalt-based catalysts in acidic environment. *Nat. Commun.* **2024**, *15*, 3067.
[38] Lu, Q.; Liu, J. J.; Zou, X. H.; Huang, B. R.; Wu, W. X.; Yin, J.; Liu, Z. Q.; Wang, Y. Breaking the activity-stability trade-off of RuO_2 via metallic Ru bilateral regulation for acidic oxygen evolution reaction. *Angew. Chem., Int. Ed.* **2025**, *64*, e202503733.
[39] Shao, T.; Geng, W.; Qin, X.; Yue, S.; Cao, R.; Cao, M. Synergy of sub-nano iridium clusters and cucurbit[6]uril-derived carbon boosts acidic water splitting. *Nano Res.* **2025**, *18*, 94907716.
[40] Wu, M.; Fan, Y. Y.; Huang, Y.; Wang, D. X.; Xie, Y.; Wu, A. P.; Tian, C. G. Synergistic Ru/RuO_2 heterojunctions stabilized by carbon coating as efficient and stable bifunctional electrocatalysts for acidic overall water splitting. *Nano Res.* **2024**, *17*, 6931–6939.
[41] Li, A. L.; Kong, S.; Guo, C. X.; Ooka, H.; Adachi, K.; Hashizume, D.; Jiang, Q. K.; Han, H. X.; Xiao, J. P.; Nakamura, R. Enhancing the stability of cobalt spinel oxide towards sustainable oxygen evolution in acid. *Nat. Catal.* **2022**, *5*, 109–118.
[42] Schulze, D. G.; Sutton, S. R.; Bajt, S. Determining manganese oxidation state in soils using X-ray absorption near-edge structure (XANES) spectroscopy. *Soil Sci. Soc. Am. J.* **1995**, *59*, 1540–1548.
[43] Soderholm, L.; Antonio, M. R.; Williams, C.; Wasserman, S. R. XANES Spectroelectrochemistry: A new method for determining formal potentials. *Anal. Chem.* **1999**, *71*, 4622–4628.
[44] Rehr, J. J.; Albers, R. C. Theoretical approaches to X-ray absorption fine structure. *Rev. Mod. Phys.* **2000**, *72*, 621–654.
[45] Weng, Z.; Wu, Y. S.; Wang, M. Y.; Jiang, J. B.; Yang, K.; Huo, S. J.; Wang, X. F.; Ma, Q.; Brudvig, G. W.; Batista, V. S. et al. Active sites of copper-complex catalytic materials for electrochemical carbon dioxide reduction. *Nat. Commun.* **2018**, *9*, 415.
[46] Yu, G.; Li, R. L.; Hu, Y. M.; Lin, X. G.; Lin, Z.; Wu, D. Y.; Wang, G. M.; Hong, X. Supporting IrO_x nanosheets on hollow TiO_2 for highly efficient acidic water splitting. *Nano Res.* **2024**, *17*, 6903–6909.
[47] Wang, Z. C.; Xu, W. J.; Chen, X. K.; Peng, Y. H.; Song, Y. Y.; Lv, C. X.; Liu, H. L.; Sun, J. W.; Yuan, D.; Li, X. Y. et al. Defect-rich nitrogen doped Co_3O_4/C porous nanocubes enable high-efficiency bifunctional oxygen electrocatalysis. *Adv. Funct. Mater.* **2019**, *29*, 1902875.
[48] Niu, H. J.; Ran, N.; Zhou, W.; An, W. X.; Huang, C. X.; Chen, W. X.; Zhou, M.; Lin, W. F.; Liu, J. J.; Guo, L. Synergistic atomic

environment optimization of nickel-iron dual sites by Co doping and Cr vacancy for electrocatalytic oxygen evolution. *J. Am. Chem. Soc.* **2025**, *147*, 2607–2615.
[49] Wu, H.; Chang, J. W.; Yu, J. K.; Wang, S. Y.; Hu, Z. A.; Waterhouse, G. I. N.; Yong, X.; Tang, Z. Y.; Chang, J. B.; Lu, S. Y. Atomically engineered interfaces inducing bridging oxygen-mediated deprotonation for enhanced oxygen evolution in acidic conditions. *Nat. Commun.* **2024**, *15*, 10315.
[50] Zhang, J.; Yang, D. S.; Yang, Z.; Wang, L. L. Utilizing cationic vacancy defects to switch oxygen evolution mechanisms on atomically dispersed Ru for enhanced acidic catalytic performance. *Appl. Catal. B: Environ. Energy* **2025**, *364*, 124845.
[51] Deng, D. H.; Yu, L.; Chen, X. Q.; Wang, G. X.; Jin, L.; Pan, X. L.; Deng, J.; Sun, G. Q.; Bao, X. H. Iron encapsulated within pod-like carbon nanotubes for oxygen reduction reaction. *Angew. Chem., Int. Ed.* **2013**, *52*, 371–375.
[52] Deng, J.; Ren, P. J.; Deng, D. H.; Bao, X. H. Enhanced electron penetration through an ultrathin graphene layer for highly efficient catalysis of the hydrogen evolution reaction. *Angew. Chem., Int. Ed.* **2015**, *54*, 2100–2104.
[53] Sun, Z. Y.; Li, C.; Lin, J.; Guo, T. Q.; Song, S. J.; Hu, Y. N.; Zhang, Z. D.; Yan, W. S.; Wang, Y.; Wei, Z. H. et al. Lattice strain and Mott-Schottky effect of the charge-asymmetry Pd_1Fe single-atom alloy catalyst for semi-hydrogenation of alkynes with high efficiency. *ACS Nano* **2024**, *18*, 13286–13297.
[54] Li, Z. S.; Yu, C. L. Chapter 6-Characterization techniques and paradigms of nanomaterials. In *Nanostructured Materials*, Li, Z. S.; Yu, C. L., Eds.; Elsevier: Amsterdam, **2024**; pp 185–224.

Zhiyi Sun received his M.S. degree from Hebei University of Science and Technology and is currently a Ph.D. student at Beijing Institute of Technology. His research centers on synchrotron radiation-based XAFS characterization, to elucidate the atomic and electronic structures of single-atom catalysts and establish clear structure–performance relationships for electrocatalysis, enabling the rational design of high-performance catalytic materials.

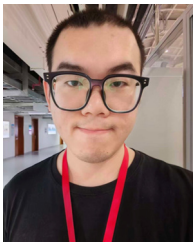

Chen Li is a doctoral student at Beijing University of Technology. The main research direction is to develop new high-performance materials for energy conversion and storage. Specifically, it refers to the use of electron microscopy, synchrotron radiation, and first principles analysis to analyze the atomic and electronic structures of materials, and to construct the performance structure relationship of materials to drive neural network models to search for potential high-performance materials.

Kun Zheng Professor/Doctoral Supervisor at Beijing University of Technology, Executive Director of the National Electronic Device Network. Received awards such as the 2011 National Excellent Doctoral Dissertation Award, the 2020 National Natural Science Second Prize, the 2022 Qilin Science and Technology Award, the 2016 Beijing Science and Technology First Prize, and the 2007 National Top Ten Scientific and Technological Advances in Higher Education Institutions. Hosted and participated in over 30 national, provincial, and ministerial level scientific research projects. His research direction is: (1) Advanced electron microscopy methods; (2) Electron microscopy research related to the structure and performance of energy and catalytic materials; (3) Synthesis, preparation, and characterization of energy and catalytic materials.

Zhuo Chen graduated from the Department of Chemical Engineering, Hunan University of Science and Technology, in 1997, and received his Master degree from the School of Materials and Metallurgy, Kunming University, in 2004, and Ph. D degree from Department of Materials Physics and Chemistry, Beijing Institute of Technology, in 2008. He did his postdoctoral research at the Department of Electronic Engineering, The Hong Kong Polytechnic University. He joined the faculty of the Department of Materials Physics and Chemistry, Beijing Institute of Technology in 2009. His research interests focus on the field of energy related photo/electrocatalysis, including solar hydrogen production, carbon dioxide conversion, and synthesis of single atom catalysts.